PAPER • OPEN ACCESS

Non-destructive analysis of Pb-acid battery positive plates, based on neutron tomography

To cite this article: Benedetto Bozzini *et al* 2024 *J. Phys. Energy* **6** 015006

View the article online for updates and enhancements.

Journal of Physics: Energy

CrossMark

PAPER

Non-destructive analysis of Pb-acid battery positive plates, based on neutron tomography

Benedetto Bozzini[1,*] ⓘ, Silvia Cazzanti[2], Raimondo Hippoliti[2], Zoltán Kis[3] ⓘ, Ludovica Rovatti[4] and Francesco Tavola[1]

1 Dipartimento di Energia, Politecnico di Milano, via Lambruschini 4, 20156 Milano, Italy
2 FIAMM Energy Technology SpA, viale Europa 75, 36075 Montecchio Maggiore (VI), Italy
3 Nuclear Analysis and Radiography Department, Centre for Energy Research, 29-33 Konkoly-Thege Miklós Street, 1121 Budapest, Hungary
4 Dipartimento di Meccanica, Politecnico di Milano, via La Masa 1, 20156 Milano, Italy
* Author to whom any correspondence should be addressed.

E-mail: benedetto.bozzini@polimi.it

Keywords: Pb-acid battery, positive plate, corrosion, neutron tomography, x-ray radiography

Abstract

Notwithstanding the in-depth understanding of lead-acid battery degradation processes developed in a time-honored field of science, there is still wide scope for knowledge-based technological advancements, in particular, targeting positive plate (PP) durability. Non-destructive imaging of the internal morphology, structure and chemistry of these components, enabled by neutron-based methods, is capable of disclosing otherwise inaccessible observables, that can form the factual basis for new pathways to device improvement. In this study, we propose a *post mortem* investigation of as-formed and electrochemically aged PPs, centered on neutron tomography and complemented by x-ray radiography and scanning-electron microscopy. These complementary imaging methods, thriving on different contrast mechanisms, allow 2D/3D position-sensitive morphological analyses of the nature and evolution of the positive active material (PAM) and of the spines of the PP, including: morphology variation, crack location, porosity distribution and identification of hydrogenated compounds. Specifically, in this work, we have pinpointed the differences in degradation modes—resulting from the application of a standard ageing protocol—of PPs fabricated in two technologically alternative ways: punching and gravity-casting, showing the superiority of the formed in terms of electrode stability upon charging abuse conditions.

1. Introduction

Lead-acid batteries (LAB) are the first rechargeable batteries ever invented. At the beginning of public electricity network, they were used as backup power supplies/storage during short peak period. Nowadays the market share of LAB is over 50% worldwide, with the largest application for starting, lighting and ignition in the automotive field, followed by an important role as energy short-time reserve in telecommunication and data network sectors [1]. LABs have low energy density combined with high surge current, monopolizing high current in-time applications. Moreover, reliability, low production cost and a well-established recycling processes make them attractive as a complementary electrochemical energy storage technology for renewables [2].

The simplest LAB electrochemical cell scheme includes PbO_2 as positive electrode active material (PAM), metallic Pb as negative electrode active material, and an aqueous solution of H_2SO_4 as electrolyte. The discharge process occurs with the conversion of anodic Pb and cathodic PbO_2 to $PbSO_4$ at the electrodes/electrolyte interface. Of course, Pb and PbO_2 are restored on electrode surfaces during charge. Depending on the details of the forming and operating conditions, the PAM typically consists of mixtures of α-, β-PbO_2 and an amorphous gel phase, essentially composed of Pb(IV) oxy-hydroxides ($Pb(OH)_4$, $PbO(OH)_2$, PbO_2, H_2PbO_3) [3]. These phases play crucial complementary roles, electronic and

architectural, in essence, that control the functional properties of the PAM. The Pb(IV) oxy-hydroxide, if appropriately hydrated [4], is the actual electrochemically active phase, undergoing reduction during discharge. Moreover, this gel is ionically, but not electronically, conducting. Mechanical consistence of the PAM composite is ensured by the α-PbO$_2$ phase, which plays the structural role of a binder. Instead, the β-PbO$_2$ variant exhibits fine-grained, loose aggregates, with poor mechanical properties. From the point of view of electronic conductivity, α-PbO$_2$ is essentially insulating, while β-PbO$_2$ exhibits a high conductivity and acts as the phase ensuring electronic contact to the electrochemically active gel phase. Jointly, α- and β-PbO$_2$ act as a Pb(IV) reservoir for reduction, occurring through the gel phase during discharge. Similarly, these two crystalline phases, in proportions that depend on the details of the charging process and the state of the material, reform from the gel phase during charging. Thus, the relative amounts and distribution of α and β crystalline zones influence LAB performances [5, 6].

The grids supporting the active materials—applied in the form of pastes—consist of Pb alloys with a range of alloying elements (e.g. C, Sb, Sn, As, Ag, In, Se, Te, Ce (e.g. [7, 8])), meant to impart solid-solution hardening and corrosion resistance.

Although LABs of different technologies have been on the market for more than one century, research and development are still warranted for at least three reasons: (i) understanding of degradation processes; (ii) optimization of cell components for traditional applications and (iii) improvement of systems for new applications, such as home- and grid-storage. As detailed below in this section, the objective of this research is to contribute to the mechanistic understanding of positive-plate (PP) degradation, on the basis of non-destructive imaging, combined with traditional SEM microscopy. Specifically, we resorted to neutron tomography (NT), complemented by x-ray radiography (XR), for the assessment of the internal structure of pristine and aged PPs produced with two alternative technologies and aged electrochemically, according to European commission standards.

As far as degradation mechanisms are concerned, the PP is affected by several processes involving both the PAM and the spines. PAM degradation, often addressed as PAM softening and shedding, occurs through: (i) decrease of cohesion among PbO$_2$ particles and between PbO$_2$ and the grid [9, 10]; (ii) decrease of the PAM particle dimensions, resulting in weaker cohesion; (iii) increase of the relative fractions of β- and α-PbO$_2$, coupled with PAM shape changes [11, 12]; (iv) presence of PbSO$_4$ crystallites, precipitated from the solution phase after charge [13]; (v) formation of less dense, amorphous PbO(OH)$_2$—Pb(OH)$_4$ phase domains, exhibiting proton conductivity, but electronically insulating, that strongly contribute to softening [3, 14] and, finally (vi), the oxygen evolution reaction (OER), causing mechanical damage to the PAM [15]. PAM degradation is often counteracted by use of additives [16].

Spine corrosion, instead, involves degradation phenomena related to coupled electrokinetic, mechanical and solution-chemistry factors of grid electrochemistry, mainly: (i) electrochemical attack [17]; (ii) stress-corrosion cracking and corrosion-enhanced creep [17] and (iii) Pb passivation by PbO$_2$. Passivation on the one hand, imparts corrosion protection, but, on the other hand, gives rise to layers that are more prone to cracking and pinhole formation [18]. So far, these damaging processes have been characterized on the basis of electrochemical measurements, optical and electron microscopy, XRD and XPS. These imaging methods can disclose a wealth of physico-chemical and structural details with micrometric and sub-micrometric spatial resolution, but require cross-sectioning of the material investigated. An intrinsic drawback of these approaches is that the necessary metallographic preparation processes are destructive and can induce damaging artefacts. A leap forward in the understanding of spine/PAM corrosion can be enabled only by non-destructive methods. Very recently, a pioneering paper has appeared, using x-ray tomography to follow the morphology evolution of a model Pb-acid battery *in operando* [19]. Unlike x-rays, owing to the properties of neutrons to interact with atomic nuclei, neutron-based imaging, in principle allows the non-destructive 3D characterization of real-scale Pb-based electrodes and even full cells. In fact, compared to x-rays, the way larger inspectable volume of the battery with neutrons counterbalances the limitations in spatial resolution. The very first example of a neutron transmission study of LABs is the full-battery radiography investigation described in [20], enabled by the large contrast between Pb and water. This work showed a relationship between the amount of hydrogen present in a sample measured by neutron transmission, and the proportion of reduced lead present determined by chemical analysis. However, this pioneering study did not give any position information of the type we are providing in the present 3D imaging investigation. Beyond imaging, other neutron-based methods, such as neutron powder diffraction [21] and inelastic neutron scattering [22] have been employed for the study of PAM structure [21] investigated the crystal structure of Pb^{4+} oxides prepared chemically and as electrochemically formed battery plates and subsequently aged with different numbers of cycles. This study enabled the detection of the presence of hydrogen and allowed to determine the crystallite dimensions, but was not conclusive regarding structure assignment, owing to difficulties in the refinement, caused by extensive defects, small-size nonspherical crystallites and departures from the orthorhombic structure. In this work, no

position-dependent information was sought after. The investigation described in [22] is based on the *in operando* acquisition of 2D neutron transmittance time series in specially designed cells This work provides some positional information, but its focus is on electrolyte management during cell operation.

Certainly, neutron imaging is the technique of choice for the study of LAB components and cells, however x-ray methods can yield complementary information. In fact, the very different and anticorrelated attenuation of neutrons and x-rays by Pb and H enables rich bi-modal contrast imaging, that we have exploited in this investigation.

In the present study, we propose, for the first time, an NT investigation of intact PPs, endeavoring to assess the internal structure of the PAM (pore formation) and spine/PAM decohesion of real battery electrodes—fabricated with two alternative metallurgical methods—subjected to harsh electrochemical testing conditions, representative of recharge abuse. Our study is complemented by XR—aimed at pinpointing spine and PAM cracking—and cross-sectional SEM imaging, to disclose details of the spine/PAM interface: grid shape variation, corrosion depth, mode and mechanism, corrosion layer nature and thickness.

2. Materials and methods

2.1. PP fabrication and electrochemical ageing
FIAMM Energy Technology SpA provided full PPs, fabricated by the punching and gravity casting methods. Gravity casting (henceforward referred to as *G*) is the best-established discontinuous Pb-alloy fabrication technology, while punching (indicated by *P* in the rest of this work) is a relatively recent technology, bearing promise of higher productivity with better flexibility in the fine-tuning of the positive grid thickness [23–26]. The PPs considered in this study were real practical samples of size (12.5 cm × 14.5 cm × 0.2 cm), with rectangular grids bearing diagonal spines diverging from the lug: a typical sample is depicted in figure 1. The spine material was a classical Pb-Ca-Sn alloy for battery applications. The PPs were studied in the as-formed and electrochemically aged conditions. Ageing was performed according to the EN-50342 standards for LABs: batteries in charged conditions were thermostated in water bath at 60 °C and overcharged at 2.4 V per cell for 21 and 42 d. The testing conditions are summarized in table 1, in which also the sample codes are provided. The rationale underlying this standard is that the electrochemical interaction between the spines and PAM determines battery performance and service life [10, 25, 27]. For completeness, a set of PPs in the same electrochemical conditions were also studied after mechanical removal of the PAM. Coupons for NT, XR and SEM imaging were cut from the PPs as shown in figure 1(b).

2.2. NT
NT measurements were carried out at the radiography/tomography station of the budapest neutron center [28]. During the tomography, a series of 601 projections was acquired with 0.30° angular increments over 180°. The beam was delivered through the radial thermal neutron channel No. 2 of the 10 MW VVR reactor. The white beam was filtered by a 150 mm long sapphire crystal filter to provide a more thermal beam, with a thermal neutron flux of 2.92×10^7 n cm^{-2} s^{-1} at the sample position (the epithermal and fast parts of the beam were effectively suppressed to 8.19×10^3 n cm^{-2} s^{-1} and 8.36×10^5 n cm^{-2} s^{-1}, respectively). The exposure time was 60 s for each 16-bit projection image, requiring 10 h of acquisition time. The object-to-screen distance was set to 25 mm to provide the best achievable spatial resolution during the rotation. For the used setup, employing a 100 μm thick LiF/ZnS(Cu) scintillator screen, the spatial resolution is 250 μm. The imaged coupons were cut from the lug side (figure 1(b), red zone) and had dimensions of 3.5 cm × 11 cm × 0.2 cm and 2 cm × 9 cm × 0.2 cm for *G* and *P* series, respectively. Tomographic 3D renderings of the samples analyzed are reported in section 3.3. The slight differences in size do not impact the imaging quality and provide a large intact volume of material for non-destructive analysis. The coupons for NT were wrapped in Teflon foils, to avoid contamination of the sample stage with Pb-containing debris, and fixed onto Al supports. Image processing and analysis were carried out with the FIJI, Octopus, KipTool and VGStudio MAX software. The raw 2D images were cropped, noise filtered, and corrected for camera dark current and flat-field before being reconstructed into 3D tomographic slices with a filtered back-projection algorithm. In this way, the imaging results, encoded as grayscale values, were converted into the 3D map of local linear attenuation coefficients, combining the absorption and the scattering effects of the sample materials. The resulting horizontal slices were then further filtered using an inverse scale space algorithm, which effectively preserves the edges. During the subsequent generation of 3D renderings, we applied a non-planar projection, to get rid of the slight, but non-uniform bending of the objects, resulting in better evaluable virtual items with planar geometry. The VGDefX analysis module of the VGStudio MAX software was used for the quantitative analysis of the pores and the voxel volumes. Based on the grayscale value distributions, we applied maximum and minimum threshold levels of 0.27 and 0.31, respectively, below and above which the areas were assigned to pores and high grayscale value areas. To avoid the biasing effect of the
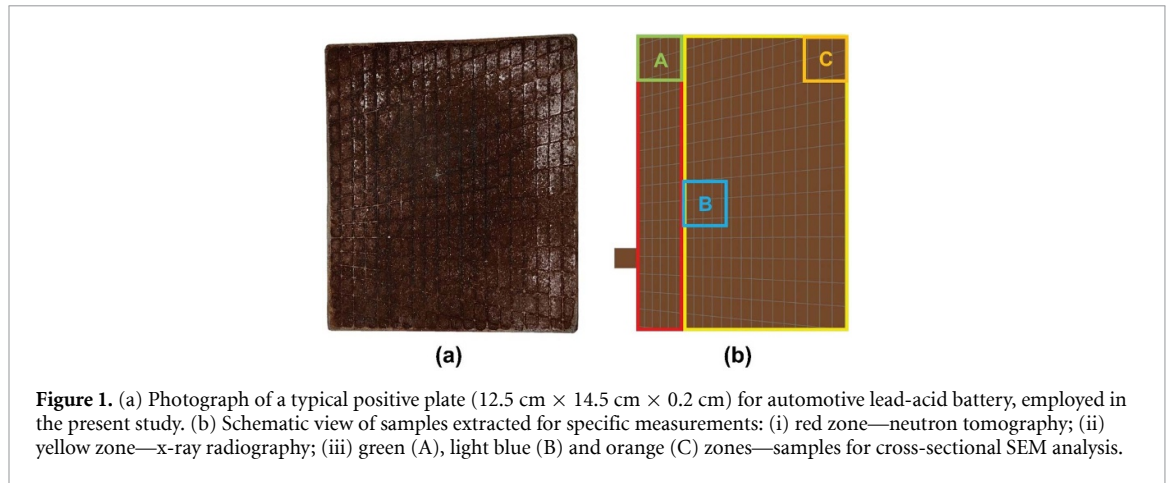
Figure 1. (a) Photograph of a typical positive plate (12.5 cm × 14.5 cm × 0.2 cm) for automotive lead-acid battery, employed in the present study. (b) Schematic view of samples extracted for specific measurements: (i) red zone—neutron tomography; (ii) yellow zone—x-ray radiography; (iii) green (A), light blue (B) and orange (C) zones—samples for cross-sectional SEM analysis.

Table 1. Samples investigated: grid fabrication technique, testing time and ageing protocol. Testing according to the EN-50342 standard was carried out by overcharging at 2.4 V at 60 °C for the indicated number of days.

Sample code	Grid fabrication	Testing time	Electrochemical ageing protocol
P_{AF}	Punching (P)	Pristine condition	As formed
P_{21}	Punching (P)	21 d	EN-50342
P_{42}	Punching (P)	42 d	EN-50342
G_{AF}	Gravity casting (G)	Pristine condition	As formed
G_{21}	Gravity casting (G)	21 d	EN-50342
G_{42}	Gravity casting (G)	42 d	EN-50342

damaged volumes encompassing features resulting from the mechanical separation of the coupon, we defined region of interest (ROI) areas with two different volumes. The larger and smaller ROIs were applied for G and P coupons, respectively, to cover the largest undamaged volumes. The minimum evaluable pore size was 0.015 mm^3 ($=0.25^3$ mm^3). It is worth noting that the feature extraction process of the VGStudio MAX software intrinsically does not give the possibility of evaluating error estimates for porosity descriptors, because it classifies the voxels as belonging to the pore phase or otherwise. This means that the porosity value for a given volume is a deterministic value, of course, depending on the parameters used in the pore analysis module, but not on the measured data. The uncertainty in porosity estimate thus depends on the choice of data processing parameters and it is not a property of the sample and of the measurement. We applied the same parameters throughout the whole evaluation process for the plates to ensure consistency of the data.

2.3. XR
XR was performed with a Seifert Eresco 65MF4 waygate technologies tube, with a 3 mm focal spot diameter, with voltage and current set to 180 kV and 2.5 mA, respectively. The source-to-detector distance was fixed to 700 mm and the exposure time was adjusted in the range 60–145 s, to optimize spatial resolution and contrast. Radiographs were recorded by a flat panel detector and subsequently digitized.

2.4. SEM characterization
3 cm × 3 cm × 0.2 cm coupons were cut from the PPs (figure 1(b), zones A-C), embedded in two-component Araldite Transparent resin (Hitech Europe epoxy), hardened overnight in a water bath, to ensure efficient heat removal, and sectioned with a Metkon Micracut 202 automatic cutting machine. The three regions selected for sampling correspond to representative nominal high (B), intermediate (A) and low (C) current density zones. The cross sections were manually polished with a specifically optimized procedure, consisting of: (i) sequential grinding, with a Hitech Europe MP3-11T polishing machine, using SiC abrasive papers of grit numbers: 400, 600, 800, 1200 and (ii) fine lapping, with the MP 22–22V machine, with 0.05 μm colloidal alumina suspension and 1 μm diamond paste. This polishing procedure yielded high-quality cross-sections, without PbO contamination: full operating details are reported in table A1 of the appendix. Each sample for SEM imaging contained three spines, all of which were examined, to ensure statistically robust metallographic observations. Regarding replicated observations, only a limited number of outliers was found, due to metallurgical preparation artefacts, connected to the reaction between the polishing media and lead grid adjacent to the corrosion layer (type 17 corrosion feature, see the list of corrosion features in the appendix). The presence of these outliers does not affect the clearcut scenario

emerging from the extensive and consistent corpus of SEM images. Samples of the PPs, after mechanical removal of the PAM were prepared in the same way. The SEM characterization was performed with a Zeiss EVO 50 SEM, equipped with energy-dispersive x-ray spectroscopy (EDS) microprobe. Both secondary (SE) and backscattered electrons (BSE) were employed to reveal sample features with optimized contrast.

3. Results and discussion

The primary aim of the present study is to prove for the first time the capability of NT to assess and characterize the corrosion features of PPs and to correlate them with the grid fabrication route and the electrochemical ageing conditions. The investigation started with the classical, SEM/EDS-based, metallographic approach (section 3.1). This method can disclose a wealth of morphological information, though at the cost of generating artefacts. The sample-penetration properties of neutrons, combined with the non-destructive nature of neutron imaging were thus employed (section 3.3) to extend the investigation of LAB corrosion. Higher-resolution, but lower-penetration x-rays were also used for complementary XR imaging (section 3.2).

3.1. SEM imaging of spine and spine/PAM interfaces

As commented in the introduction, cross-sectional SEM imaging, combined with optical microscopy (OM), can be regarded as the state-of-the-art approach to the investigation of PP corrosion. Notwithstanding the drawback of potential metallographic preparation artefacts, SEM and OM enable access to micrometric and submicrometric corrosion features. A further issue of cross-sectional imaging is that metallographic artefacts are sometimes difficult to discern from corrosion features, also because appropriate contrast is typically achieved through etching. Notwithstanding these downsides, the key advantage of SEM and OM is that they give access to defects of extremely small dimensions. Nevertheless, extreme localization might mislead the investigation, tending to overestimate the importance of features that are morphologically evident, but the functional impact of which could be negligible. In any case, micrometric defects inside large-dimension samples are not currently accessible either by NT of by x-ray tomography. Thus, in this study, we employ SEM imaging to align our study with state-of-the-art approaches to the materials-science topic considered, specifically to characterize the localization of corrosion at the spine/PAM interface, to observe geometrical details of spine/PAM cohesion.

SEM imaging was performed on replicated samples, as detailed in section 2.4, allowing to cogently associate the corrosion morphology with the sample conditions. A general comment, valid for all examined samples, is that in no case we could observe a correlation between the nominal current density distribution and the corrosion morphology. Thus, the harsh corrosion conditions imposed, seem to overwhelm electrochemical details, that have been considered in the modeling literature on PP corrosion both at the spine [18] and whole-electrode [29] scales. For this reason, we report only a selection of representative micrographs, corresponding to location B (high nominal current density). SEM micrographs of *P*- and *G*-type samples are reported in figures 2 and 3, respectively. In the following discussion, we shall be referring to the types of corrosion features expounded systematically in the appendix.

The Pb-alloy spines of sample P_{AF} (figure 2(a)) are essentially uncorroded, showing just some traces of incipient oxide layer formation at spine/PAM interface. Traces of mild corrosion, resulting from the electrochemical conditions prevailing in the curing-soaking-formation process, have been reported [5, 6, 30]. As far as the spine/PAM interface is concerned, PAM voids and decohesion in correspondence of spine can be noticed.

After 21 d of anodic polarization, the *P* grid (sample P_{21}, figure 2(b)) shows a clear corrosion layer, consisting of two connected sub-layers, separated by an internal boundary (type 2 corrosion feature): in keeping with the SEM contrast, EDS analyses confirm the typical $Pb/PbO/PbO_2$ layering. Fissure cracks (type 11 corrosion feature) form perpendicularly to the external corrosion layer. Sparse voids—better highlighted by complementary BSE/SE contrast—appear at the internal boundary between the corrosion layer and the uncorroded spine core (type 4 corrosion feature), accompanied by the formation of a porous, micrometric interfacial layer between grid and corrosion layer (type 3 corrosion feature). Overall, a limited additional spine/PAM decohesion develops as a result of corrosion under these conditions.

After 42 d of anodic polarization, the *P* grid (sample P_{42}, figure 2(c)) exhibits a notable progress of corrosion attack, with respect to condition P_{21}, characterized by notably extended spine/PAM decohesion. Similarly to P_{21}, the double corrosion layer forms (type 2 corrosion feature) corresponding to an increasing degree of oxidation of Pb from the spine core to the external sub-layer. Again, a porous interfacial layer forms between the grid and the corrosion layer (type 3 corrosion feature). At the internal boundary between the corrosion layer and the uncorroded spine core, connected and larger voids (type 4 corrosion feature) replace the sparse voids characteristic of P_{21}. In addition, fissure cracks perpendicular to the external corrosion layer
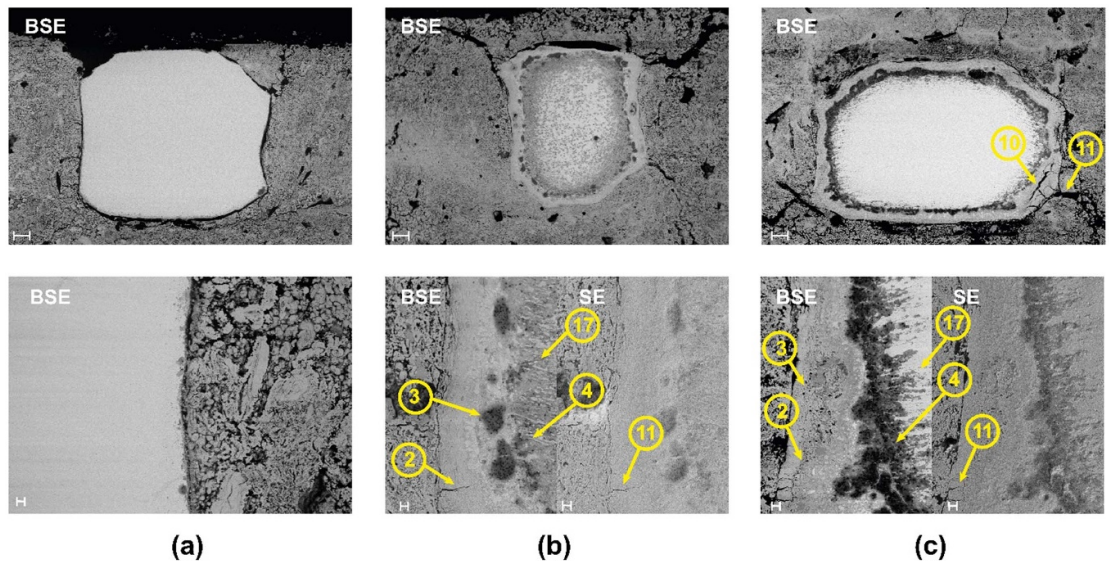
Figure 2. Representative SEM cross-sections of the spine/PAM zones of punched (*P*-type) positive plates in the following conditions: (a) P_{AF} as-formed; (b) P_{21} electrochemically aged for 21 d; (c) P_{42} electrochemically aged for 42 d (details in text). Backscattered electrons (BSE) contrast modes, except image marked SE: secondary electrons contrast mode. The scale-bars in first and second rows correspond, respectively to 100 and 20 μm.
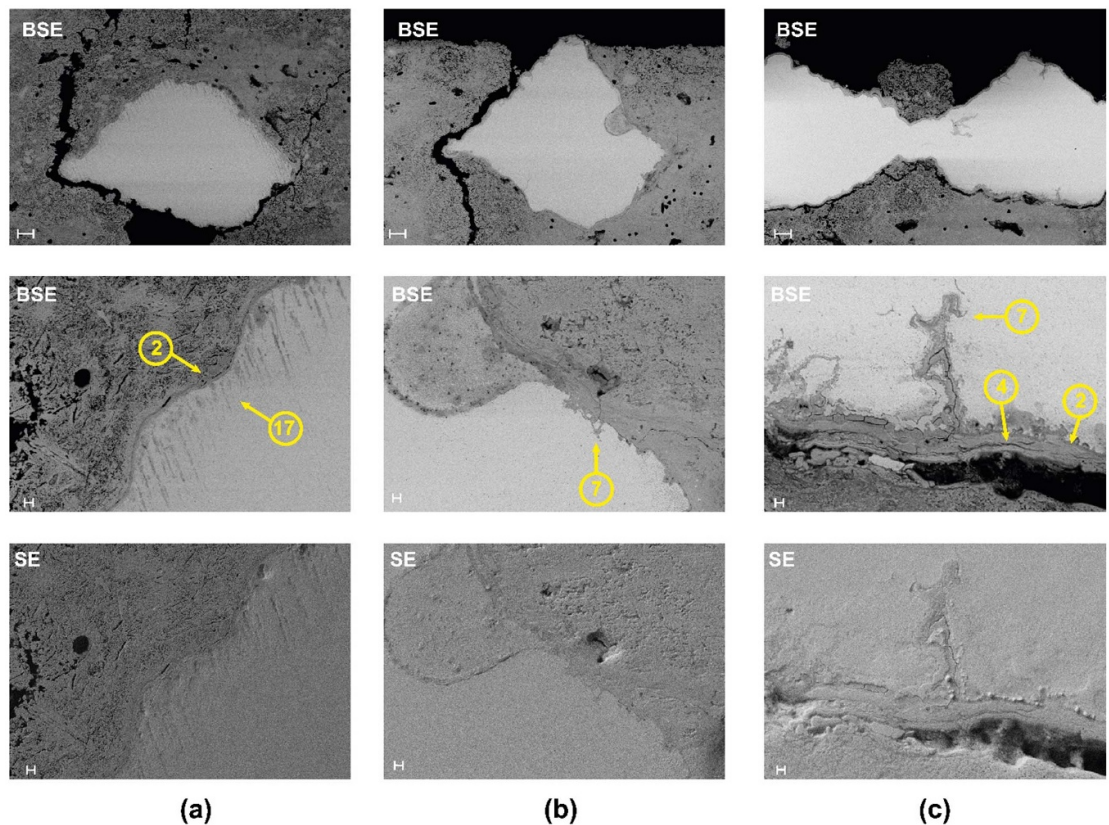

Figure 3. Representative SEM cross-sections of the spine/PAM zones of gravity-cast (*G*-type) positive plates in the following conditions: (a) G_{AF} as-formed; (b) G_{21} electrochemically aged for 21 d; (c) G_{42} electrochemically aged for 42 d (details in text). Backscattered electrons (BSE) contrast modes, except image marked SE: secondary electrons contrast mode. The scale-bars in first row corresponds to 100 μm and those in the second and third rows to 20 μm.

(type 11 corrosion feature) are found, with higher density than in sample P_{21}. Moreover, cracking at the internal boundary within the two corrosion layers (type 10 corrosion feature) appears.

Comparing figures 2 and 3, for samples *P* and *G*, respectively, one can conclude that *G* electrodes are globally characterized by notably lower corrosion attack and more extensive spine/PAM decohesions. The
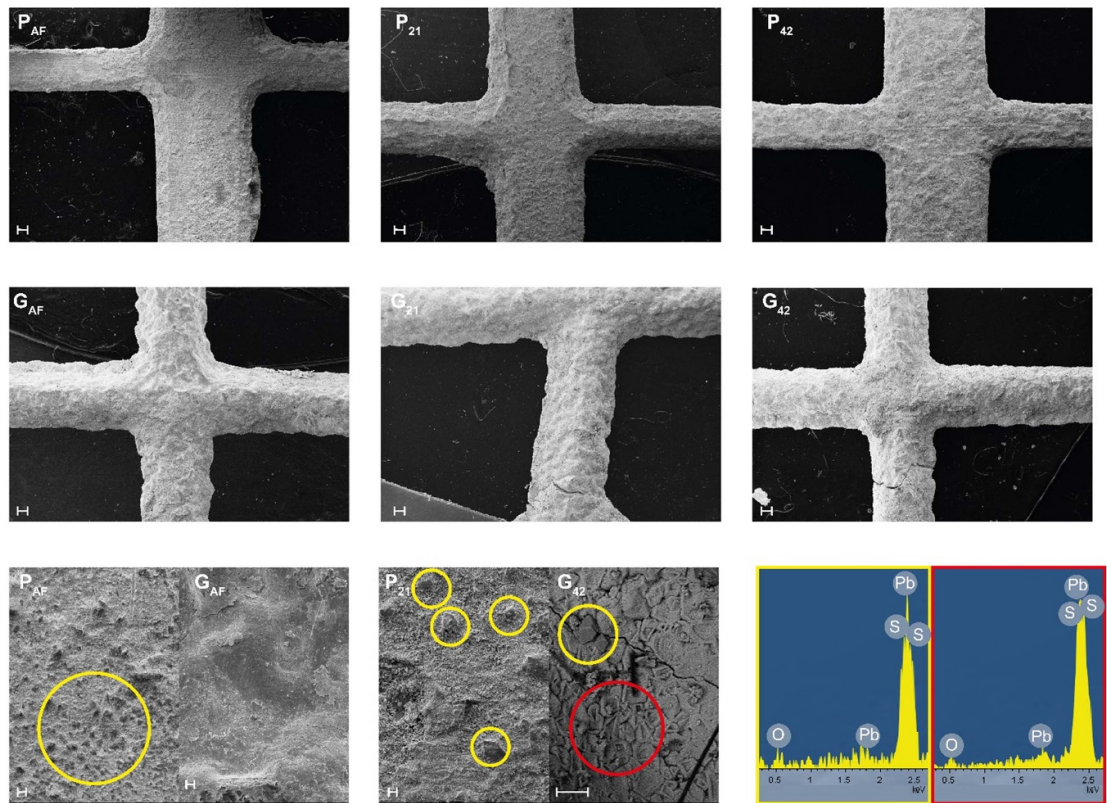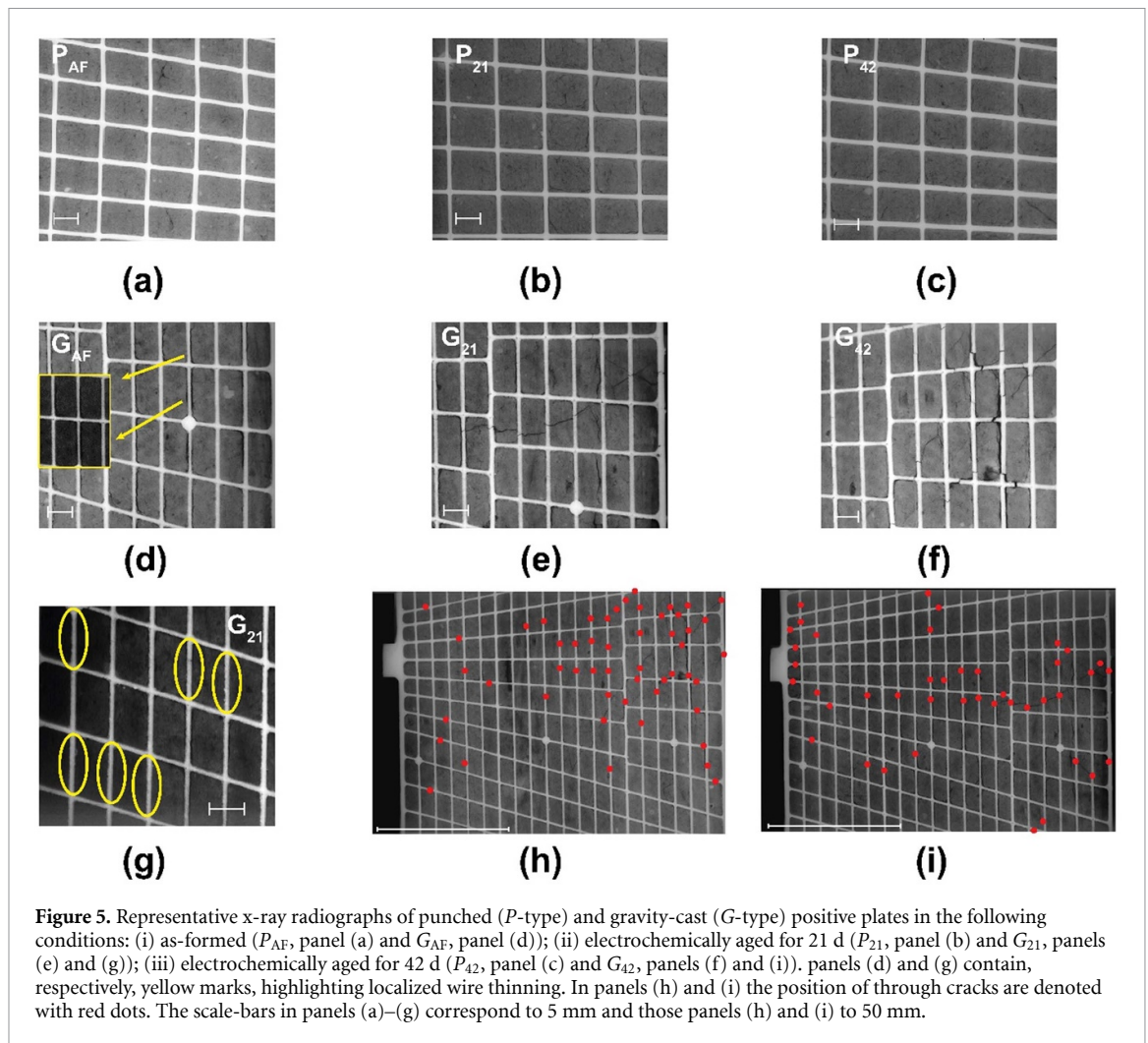
Figure 4. Representative SEM backscattered electron images of the surface of positive-plate spines after mechanical removal of the PAM. Punched (*P*) and gravity-cast (*G*) positive plate grids in the following conditions: (a) G_{AF} as-formed; (b) G_{21} electrochemically aged for 21 d; (c) G_{42} electrochemically aged for 42 d. PbSO$_4$ crystals are highlighted in yellow. The scale-bars in first and second rows correspond to 200 μm and those in the third row to 20 μm. The plot at the bottom-right reports EDS spectra for a typical PbSO$_4$ grains (features highlighted in yellow) and patches (region highlighted in red).

latter defect does not seem to correlate with the imposed electrochemical conditions, but rather to the electrode preparation process. In particular, corrosion product films are notably thinner in *G* than in *P* samples and the thin corrosion layer seems compact and without sub-layers (type 1 corrosion feature) in G_{AF} and G_{21} conditions. An internal boundary within corrosion layer (figure 2(a), type 2 corrosion feature)—accompanied in some positions by cracking at the at the internal boundary (type 10 corrosion feature) and sparse voids/pores (type 4 and 5 corrosion features) -, becomes clearly visible only after 42 h of attack. Finally, oxide fingers, the extent of which correlates with the aggressiveness of attack conditions (type 7 corrosion feature, see figures 3(b) and (c) for samples G_{21} and G_{42}, respectively), are found in *G* samples, but not in *P* ones.

To complete the analysis of the diffuse region between the spine and the PAM, we also carried out SEM imaging of the surface of the spine after mechanical removal of the PAM: a representative selection of results is reported in figure 4. In all cases, in keeping with literature studies that implemented this approach [31–33], the morphology is characterized by a thick oxide layer, with embedded PbSO$_4$ crystals (see zones highlighted in yellow), residuating from the formation process [34]. In *P*-type samples, regardless of the corrosion mode, the oxide layer is characterized by grains some tens of μm in size, embedded in a background of finer oxides. Instead, the oxide layers found in *G* samples exhibit monodisperse globular PbSO$_4$ crystallites ca. 20 μm in diameter. Moreover, G_{21} and G_{42} samples show evident spine cracks, the linear density of which increases with the degree of corrosive attack.

3.2. XR of whole PPs

XR of complete PPs enables accurate and comprehensive, non-destructive inspection at grid scale of the cracking phenomena observed locally by SEM. This conveys complementary information jointly on the spine and PAM components of the PP. Typical images are reported in figure 5. It is worth noting here that excellent prior work exists on x-ray tomography and radiography of LABs, in particular, focussing on plate porosity [35]. This work classically pinpoints the advantages of x-ray imaging compared to neutron imaging, in terms of spatial resolution, allowing the analysis of a wider pore volume range. However, the downside of x-ray tomography is the very small size of the investigated volume (typically some tens of mm^3) of the battery

Figure 5. Representative x-ray radiographs of punched (*P*-type) and gravity-cast (*G*-type) positive plates in the following conditions: (i) as-formed (P_{AF}, panel (a) and G_{AF}, panel (d)); (ii) electrochemically aged for 21 d (P_{21}, panel (b) and G_{21}, panels (e) and (g)); (iii) electrochemically aged for 42 d (P_{42}, panel (c) and G_{42}, panels (f) and (i)). panels (d) and (g) contain, respectively, yellow marks, highlighting localized wire thinning. In panels (h) and (i) the position of through cracks are denoted with red dots. The scale-bars in panels (a)–(g) correspond to 5 mm and those panels (h) and (i) to 50 mm.

material, as well as the necessity, in most cases, or removing structural parts of the plate, such as the lug and the frames, to render the sample penetrable by x-rays. Of course, this raises repeatability and representativity issues similar to those demanded by SEM and OM imaging.

Coherently with SEM analyses of section 3.1, the as-formed *P*-type electrode (P_{AF}, panel (a)) shows limited defectivity, characterized by minor PAM thinning and hardly any spine/PAM decohesion. After electrochemical ageing for 21 (P_{21}, panel (b)) and 42 h (P_{42}, panel (c)), x-ray radiographs disclose that both PAM and spine/PAM interfaces of the P_{21} sample are still almost intact. Instead, moderate spine cracking, PAM thinning and spine/PAM decohesion can be found in sample P_{42}.

At variance with P_{AF}, the G_{AF} sample (panel (d)) exhibits extensive spine thinning and spine/PAM decohesions, as well as incipient spine cracking. After electrochemical ageing, both spines and PAM of the G_{21} and G_{42} samples (panels (e) and (f), respectively) are extensively cracked. Many cracks extend across both PAM and spine, and show localized spine thinning, highlighted with yellow marks in panel (g). Ageing for 42 h leads to significantly more extensive damaging than for 21 h. The cracking patterns of samples G_{21} and G_{42} are shown in panels (h) and (i), respectively, where the red dots denote through cracks in spines.

Interestingly, the progress of the spine corrosion as characterized by local SEM imaging does not correlate with deterioration of the functionally relevant plate scale. The spines of *P* samples exhibit notably more evident corrosion features than those of *G* samples, but the global damaging of both spines and spine/PAM interfaces is much more severe in *G*-type PPs. This conclusion leads to a note of caution in the use of highly localized corrosion probes and highlights the importance of global corrosion imaging, spanning reasonably large portions of the real battery component.

3.3. NT

Figure 6 reports a representative selection of NT cuts of as-formed and electrochemically aged PPs. The spines and the PAM, as well as their defectivity, can be clearly assessed. In all images, with different density and distribution, four key features can be noticed: (i) PAM porosity, (ii) spine/PAM decohesions, (iii) PAM
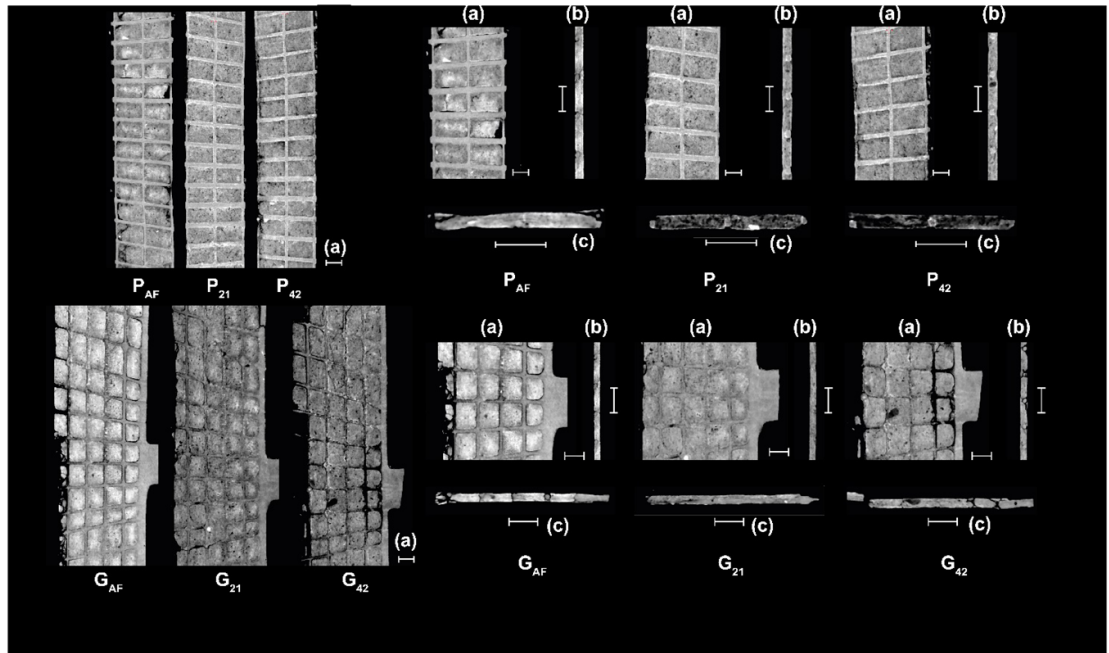
Figure 6. Representative neutron tomographic (NT) frontal (a), sagittal (b) and transversal (c) cuts of *P* and *G* samples, as-formed (AF: P_{AF}, G_{AF}) and electrochemically aged for 21 (P_{21}, G_{21}) and 42 d (P_{42}, G_{42}). The scale-bars correspond to 5 mm.

cracking and (iv) presence of highly attenuating regions. The observation of features (i)–(iii) corroborates the findings of 2D XR, expounded in section 3.2, and provides additional qualitative and quantitative detail, thanks to the 3D nature of the tomographic information. Point (iv) is exclusive of the contrast mechanism enabled by neutrons. Porosities and cracking are the result of PAM application and curing, while spine/PAM decohesions can result either from OER during the formation step or from the thermal curing process, whereby the faster temperature increase in the PG than in the PAM could cause water vapor bubble generation at the spine surface [34].

In the as-formed state, the 3D structure of *P* samples (P_{AF}) is characterized by the presence of extensive porosity in the PAM, while that of *G* electrodes (G_{AF}) is more compact, but exhibits a high proportion of spine/PAM decohesions and the presence of sparse cracks.

Ageing of both *P* and *G* electrodes leads to the progressive growth and coalescence of pores, with a predominance of a higher density of closed pores in *P* samples and a lower density of connected ones in *G* electrodes. In addition, *G* samples develop extensive cracking in random directions within the PAM volume, with a tendency for cracks to localize at the PAM/grid spine interface and form surface delaminations. This tendency to cracking of *G* samples correlates with evident PP softening and creep, that can be visually assessed at the plate scale [36]. Coherently with the observations of sections 3.1 and 3.2, the structure of as-formed *P* and *G* electrodes and its evolution with ageing are essentially independent on the sampling position, denoting a limited impact of the current density distribution: the same explanation provided in section 3.1 applies also here.

The NT reconstructions have been analyzed quantitatively (see section 2.2 for details) to extract information regarding porosity distribution and volume of the highly attenuating regions. The porosity distribution for all the samples investigated is depicted in figure 7, where the spatial distribution of the pores is mapped averaging over five voxels. Porosity estimators were calculated for the 3D volumes depicted in figures 7(a) and (b). These volumes cover the whole thickness of the plates but avoid the perimeter of the objects. The reason for this choice is to avoid the biasing effects resulting from cracks and grains present in these regions, that are affected by mechanical cuts. The analyzed volumes were 12.97 mm × 88.02 mm × thickness = ~2200 mm³ for the *P* series of electrodes and 23.44 mm × 88.73 mm × thickness = ~3700 mm³ for the *G* series of electrodes. Corresponding porosity estimates are summarized in figure 8. It is worth noting that the spatial distributions of the pores, imaged in figure 7, are multimodal and quite different for the two types of plates. Specifically, as detailed below, the porous regions in the *P* plates is typically less extended that in *G*-type plates. These, instead, exhibit a relatively uniform distribution without evident agglomeration. Thus the particular kind of porosity prevailing in these electrodes does not lend itself to straightforward quantification. Nevertheless, the estimate
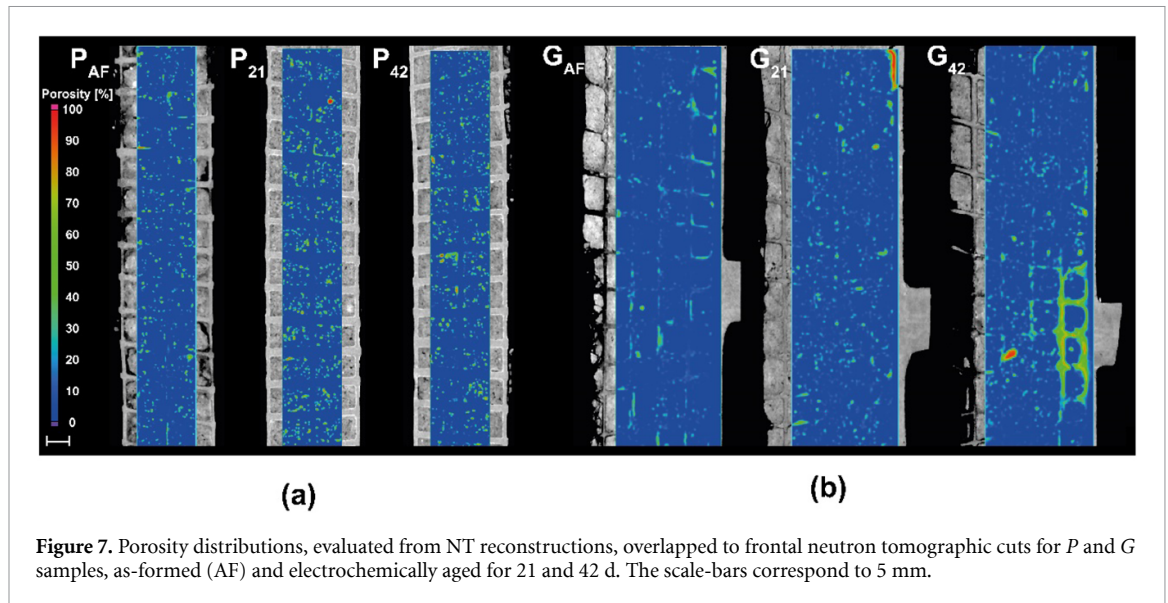
Figure 7. Porosity distributions, evaluated from NT reconstructions, overlapped to frontal neutron tomographic cuts for *P* and *G* samples, as-formed (AF) and electrochemically aged for 21 and 42 d. The scale-bars correspond to 5 mm.
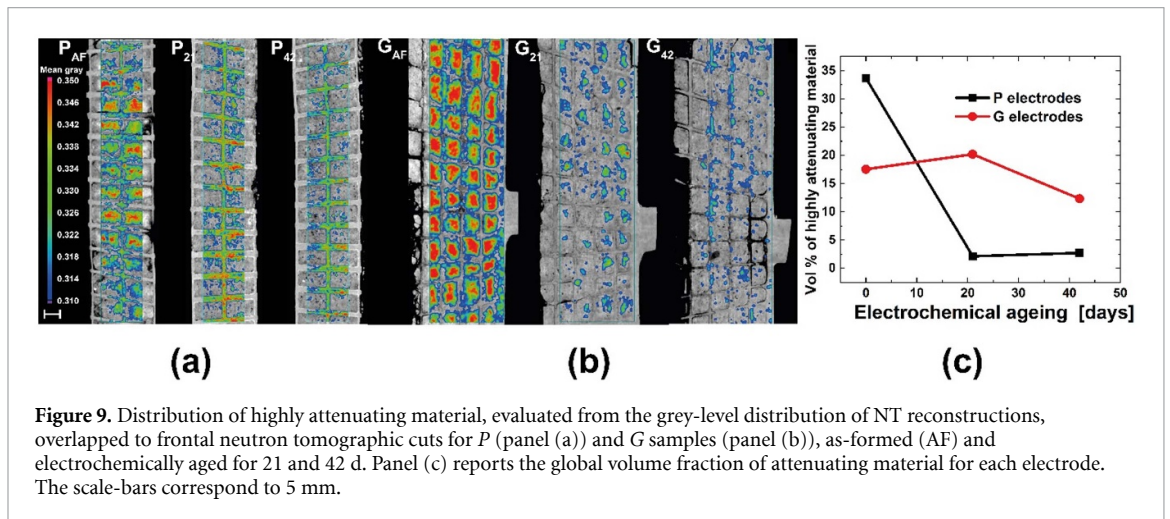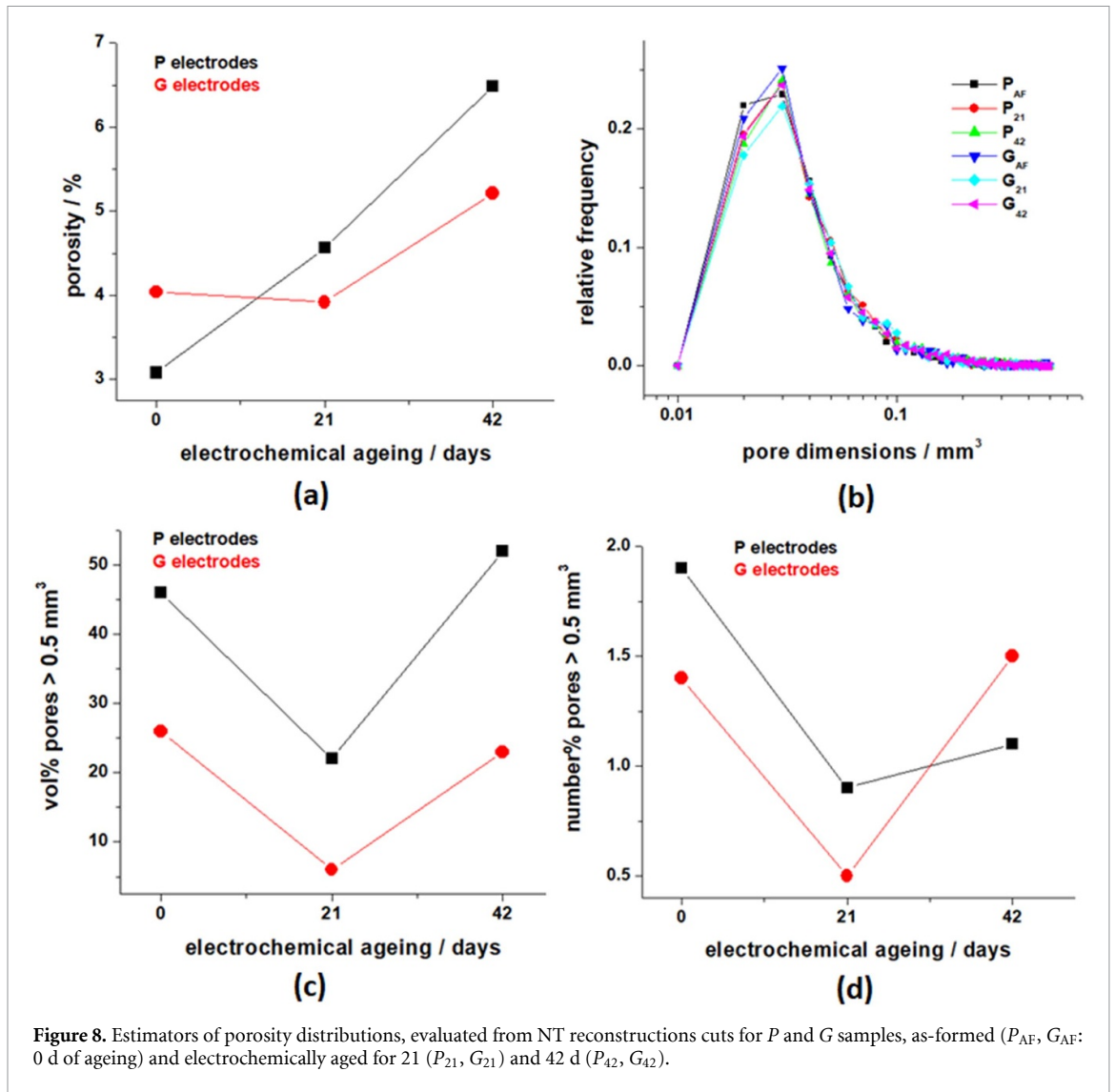
of a global porosity descriptor, such as proposed in figure 8, helps to provide a more complete, though of course not definitive, qualification of the properties of the two samples. In fact, this yields a representative scale that renders comparisons more perspicuous. It is worth recalling here that, as explained in section 2.2, the feature extraction process of tomographic data is intrinsically incompatible with the estimation of experimental error bars. Panel (a) shows that, in both types of electrodes, the porosity tends to increase with anodic polarization time. *P* electrodes have a lower porosity in as-formed conditions, but their porosity-increase rate is higher than for *G* electrodes. Having noted these differences in absolute porosity, as far as the porosity distribution and their ageing evolution are concerned, the two classes of electrodes exhibit a very similar behavior in the case of pores of dimensions smaller than 0.5 mm^3, as one can note from the curves of panel (b). The distribution of larger pores can be effectively quantified in terms of the volume and number fractions of pores with dimensions in excess of 0.5 mm^3: these values are reported in panels (c) and (d), respectively. From panel (c), one can notice that the volume ratio of the larger pores is considerable. Specifically, the relative volume of larger pores is about a factor of two larger for *P* electrodes with respect to type-*G* ones. However, as one can clearly assess from figure 7, the connected porosity is notably higher for the *G* samples. Moreover, one can notice that the structure of the void areas is different for *P* and *G* samples: in the latter, voids concentrate mainly in the vicinity of the spines, while for the former, they are more evenly distributed. These differences in morphology between *P* and *G* samples can be straightforwardly related to the fabrication process: in fact, the gravity casting method (samples *G*) is a discontinuous one, whereby the active-mass spreading step typically gives rise to heterogeneities, among which decohesions and cracks. Instead, the punching approach (samples *P*) is a continuous production, that ensures better active-mass coverage and homogeneity.

Regarding the evolution of porosity, this is found to decrease in the initial stages of electrochemical ageing, owing to the stabilization of the $PbO(OH)_2$ gel dispersion in the PAM, favouring PG/PAM cohesion. After prolonged ageing, the porosity tends to increase: this observation is consistent with the fact that, upon prolonged overcharging, $PbO(OH)_2$ can be converted back to PbO_2, thus losing the structural compaction role, attributed to a homogeneous distribution of the Pb-based gel phase [37].

Notwithstanding the quantitative differences, it is worth noting that the trend is the same for *P* and *G* electrodes, denoting that the PAM degradation mechanisms prevailing in both systems are essentially the same and are not affected by the different responses to corrosion of the spines, pinpointed in sections 3.1 and 3.2.

Regarding the relative number of pores larger than 0.5 mm^3, it should be noted that, in all cases investigated, their number is limited, amounting to around 1%, and generally slightly larger for *P* electrodes (figure 8(d)), clearly in keeping with the 3D vertical cuts shown in figure 7. Correlating with the pore dimensions, the number of larger pores decreases after the first ageing step and it grows again at more advanced stages. The same explanation given for the evolution of porosity distribution applies also here.

As noted in the description of figure 6, the presence of highly attenuating regions is characteristic of the investigated samples. This response of the samples to the neutron field, suggests that these zones are characterized by a sizable concentration of hydrogen-containing material. The 3D cuts of figure 6 and of the gray-scale distribution plots of figure 9 clearly show that these areas are typically located in the PAM for

Figure 8. Estimators of porosity distributions, evaluated from NT reconstructions cuts for *P* and *G* samples, as-formed (P_{AF}, G_{AF}: 0 d of ageing) and electrochemically aged for 21 (P_{21}, G_{21}) and 42 d (P_{42}, G_{42}).

Figure 9. Distribution of highly attenuating material, evaluated from the grey-level distribution of NT reconstructions, overlapped to frontal neutron tomographic cuts for *P* (panel (a)) and *G* samples (panel (b)), as-formed (AF) and electrochemically aged for 21 and 42 d. Panel (c) reports the global volume fraction of attenuating material for each electrode. The scale-bars correspond to 5 mm.

as-formed electrodes (samples P_{AF} and G_{AF}), while for the electrochemically aged PPs they tend to shrink and concentrate in the vicinity of the spines, progressively with the extent of ageing. Figure 9(c) evidences that the decrease of highly attenuating material volume is about one order of magnitude larger for *G*- than for *P*-type electrodes. This highly attenuating material can be identified with the amorphous

PbO(OH)$_2$—Pb(OH)$_4$ phase domains—known from the literature on the electrochemisty and structure of PAM-, an appropriate fraction of which is required for optimal performance and reported to correlate with the state-of-health (SOH) of the electrode [3, 14]. In as-formed conditions, the exact nature and distribution of hydrogenated gel depend, in a poorly understood way, on the details of the intermediate fabrication steps, chiefly: curing, soaking and electrochemical formation. In fact, during the soaking step, the gel phase formed during the preceding curing step, is transformed at the spine/PAM interface to Pb^{2+}. This is a result of the reaction of hydrogenated Pb(IV) species with the elemental Pb of the spine. The formation of Pb^{2+} from both Pb(IV) and Pb(0) species eventually leads to the precipitation of PbSO$_4$, causing gel depletion from the PAM region closer to the spine [34]. It is worth noting here that this is the first 3D imaging study of the hydrogenated gel in the PAM context. In fact, we could follow the gel distribution in the PP thanks to the hydrogen contrast enabled by thermal neutrons. Our neutron tomographic results, through the analysis of the voxels grayscale value distribution, provide the spatial distribution of the gel, allowing—by segmentation—to image solely the gel, as highlighted in figure 9. Note that, in this figure, we have left the metal plate visible exclusively to allow the localization of the gel within the PP geometry.

The pristine *P*-type (*P*$_{AF}$) electrodes show more homogeneously distributed hydrogenated gel domains, rendering the PAM structure more compact. Instead, *G*$_{AF}$ samples exhibit an uneven distribution, that could lead to the concentration of the electrochemical activity in specific regions, favoring localized damaging.

As a result of ageing of *P* electrodes, the fraction of hydrogenated gel at the PAM surface progressively decreases, while it tends to concentrate at the spine/PAM interface. Instead, in *G* samples, a progressive loss of gel from the PAM is found. These differences in gel distribution in the two types of electrodes can be explained with the tendency in aged *P* samples to concentrate the amorphous PbO(OH)$_2$—Pb(OH)$_4$ phase at the spine/PAM interface. This is due to the oxidation of the PG alloy, that releases ions, tending to hydrate, thus favoring local gel formation [5, 31], in turn, leading to improved spine/PAM cohesion.

4. Conclusions

In this work, we have shown the capability of NT, complemented with XR, of imaging large portions of intact full-sized Pb-acid battery (LAB) electrodes. This approach integrates traditional approaches, based on optical and electron microscopy of cross-sections, allowing to place local corrosion defects in the context of the full components and thus of assessing they actual functional impact. Moreover, neutron and x-ray based techniques in principle allow non-destructive imaging, thus excluding observation-induced damaging, that is typical of state-of-the-art metallographic methods. However, x-ray imaging, compared to neutron imaging, is limited if applied to large and dense objects. In fact, x-ray penetration depth a dense material, such as Pb, is way shorter than that of neutrons, typically resulting in more CT imaging artefacts, compared to that of neutrons. In addition, x-ray have no sensitivity for hydrogen. Therefore, neutron imaging is the approach of choice for providing 3D data for hydrogen-containing LaB materials, excluding observation-induced damaging. Finally, notwithstanding the lower spatial resolution currently achievable by NT, with respect to SEM, the key, functionally relevant degradation features can be accurately identified and followed.

This study is centred on the analysis of two sets of PPs, fabricated with the same materials and tested under the same, harsh electrochemical conditions, but via two different metallurgical routes: punching (P) and gravity-casting (G). In terms of resistance to functional degradation, the former fabrication method largely outperforms the latter. We have shown that imaging of the corrosion features based on SEM is not diagnostic of the actual functional damaging, that can instead be fully identified only if 3D information is available, for intact samples comprising the spine/PAM compound. The availability of this type of information allowed to discern that local spine corrosion—an aspect that tends to be overemphasized by SEM—, can have beneficial effects, leading to better-quality PAM and more stable performance of the spine/PAM interface. This conclusion has been enabled by the capability of observing, identifying and quantifying the morphochemical observables that impact concrete electrode operation, such as spine/PAM decohesion, PAM and spine thinning and cracking and the formation of open and closed pores in the PAM. Moreover, NT opens up the unique opportunity of imaging directly the 3D distribution of the hydrogen-containing electroactive amorphous phase—a highly diagnostic SOH metric—that is an otherwise experimentally inaccessible.

In conclusion, systematic application of NT bears promise of providing the morphochemical knowledge-base for the understanding of the fabrication and ageing of Pb-acid battery electrodes, with *in operando* capability, that we shall explore in a subsequent publication, based on the quantitative analysis of the functionally relevant features and their evolution upon ageing.

Data availability statement

All data that support the findings of this study are included within the article (and any supplementary files).

Acknowledgments

Appendix

List of corrosion features

Here below, we have compiled a list of the key corrosion features for PP spines and spine/PAM interfaces, based on the discussion of OM and SEM images published in [18, 25, 30, 33, 36, 38–45]. This list has been enriched also with references concerning the corrosion of Pb and Pb alloys in other fields [46]. We employ these categories to comment the SEM micrographs presented in section 3.1.

The corrosion features of the spine/PAM interface of PPs, reported in the literature, can be grouped in three categories, each with several variants, as detailed below. The three categories correspond to: (a) formation of a corrosion layer; (b) cracking of the corrosion layer and (c) spine/PAM interaction.

(a) Corrosion layer
Corrosion layers of thicknesses ranging between fractions of a μm and many tens of μm have been reported. The following charactaristics of corrosion layers have been reported.

1) Compact submicrometric/micrometrc interfacial layer between grid and corrosion layer, with no sub-layers
2) Corrosion layer, consisting of two connected sub-layers, separated by an internal boundary. The position of internal boundary with respect to the spine surface can vary.
3) Porous micrometric interfacial layer between grid and corrosion layer.
4) Voids, several microns in extent, at the internal boundary within the corrosion layer.
5) Porosity (dimensions from submicron to micrometric) within either single or double corrosion layer.
6) Oxide particles formed between spine and corrosion layer.
7) Oxide fingers penetrating the spine.
8) Corrosion propagating inside the spine, along grain boundaries.

(b) Cracking
9) Cracks perpendicular to the corrosion layer: mostly adjacent to grid-spine corners, but also at the edge of the spine.
10) Cracks at the internal boundary within the corrosion layer.
11) Fissure cracks in the external corrosion layer.
12) Extensive intergranular cracking of corrosion layer.
13) Axial cracking of oxide fingers (8), penetrating the grid.
14) Stress corrosion cracking of the spine.

(c) Spine/PAM interaction
15) Pores in PAM, possibly interacting with spine.
16) PAM-filled cracks
17) Moreover, sometimes a characteristic metallographic artefact has been reported reaction between the polishing media and lead grid adjacent to the corrosion layer, yielding an additional feature, that can be described as a staining on the internal section of the spine.

Table A1. Protocol for the preparation of SEM cross sections.

Step	Preparation	Parameters	Time
1	Embedding grid portion with Araldite Transparent Hitech Europe (80%) and REN HY 956 (20%). Put the incorporated sample inside a water bath to take temperature under control, there is risk of Pb and resin parasite reaction.	/	Overnight
2	Automatic cross cutting	Feed rate: 15 μm s^{-1} Rotational speed: 300 rpm	/
3	Mechanical polishing: abrasive paper 400 grit	Rotational speed: 100 rpm	5 min
4	Mechanical polishing: abrasive paper 600 grit	Rotational speed: 100 rpm	5 min
5	Mechanical polishing: abrasive paper 800 grit	Rotational speed: 100 rpm	5 min
6	Mechanical polishing: abrasive paper 1200 grit	Rotational speed: 100 rpm	7.5 min
7	Mechanical polishing: abrasive paper 2500 grit	Rotational speed: 100 rpm	7.5 min
8	Mechanical polishing: colloidal alumina suspension 3 μm	Rotational speed: 100 rpm	7.5 min
9	Mechanical polishing: diamond paste 1 μm	Rotational speed: <100 rpm	2.5 min
10	Mechanical polishing: diamond paste 1 μm	Rotational speed: <100 rpm	2.5 min
11	Mechanical polishing: diamond paste 1 μm	Rotational speed: <100 rpm	2.5 min
12	Mechanical polishing: diamond paste 1 μm	Rotational speed: <100 rpm	2.5 min

ORCID iDs

Benedetto Bozzini ● https://orcid.org/0000-0002-2725-9157
Zoltán Kis ● https://orcid.org/0000-0002-8365-8507

References

[1] Mohammadi F and Saif M, 2023 *e-Prime-Adv. Electr. Eng. Electron. Energy* **3** 100127
[2] May G J, Davidson A and Monahov B 2018 *J. Energy Storage* **15** 145–57
[3] Pavlov D 1992 *J. Electrochem. Soc.* **139** 3075–80
[4] Pavlov D, Bashtavelova E, Manev V and Nasalevska A 1987 *J. Power Sources* **91** 15–25
[5] Pavlov D 2017 Formation of positive lead–acid battery plates *Lead-Acid Batteries: Science and Technology* (Elsevier) pp 461–500
[6] Dimitrov M, Pavlov D, Rogachev T, Matrakova M and Bogdanova L 2005 *J. Power Sources* **140** 168–80
[7] Rogatchev T, Papazov G and Pavlov D 1983 *J. Power Sources* **10** 291–303
[8] Calábek M, Micka K, Bača P, Křivák P and Šmarda V 1996 *J. Power Sources* **62** 161–6
[9] Ruetschi P 2004 *J. Power Sources* **127** 33–44
[10] Yan J H, Li W S and Zhan Q Y 2004 *J. Power Sources* **133** 135–40
[11] Papazov G and Pavlov D 1996 *J. Power Sources* **62** 193–9
[12] Suozzo C 2008 Lead-acid battery aging and state of health diagnosis *MSc Thesis* (The Ohio State University)
[13] Yamaguchi Y, Shiota M, Nakayama Y, Hirai N and Hara S 2001 *J. Power Sources* **93** 104–11
[14] Pavlov D 2017 Fundamentals of lead–acid batteries *Lead-Acid Batteries: Science and Technology* (Elsevier) pp 33–129
[15] Nakamura K, Shiomi M, Takahashi K and Tsubota M 1996 *J. Power Sources* **59** 153–7
[16] Hao H, Chen K, Liu H, Wang H, Liu J, Yang K and Yan H 2018 *Int. J. Electrochem. Sci.* **13** 2329–40
[17] Pedro M R and Sequeira C A C 2007 *Cienc. e Tecnol. dos Mater.* 19
[18] Ball R J, Evans R, Deven M and Stevens R 2002 *J. Power Sources* **103** 207–12
[19] Stone C W, Hall C, Pohl O M, Hollenkamp A F, Newnham R H, Mahon P J and Hocking R K 2023 *J. Power Sources* **557** 232538
[20] Campillo-Robles J M, Goonetilleke D, Soler D, Sharma N, Rodríguez D M, Bücherl T, Makowska M, Türkilmaz P and Karahan V 2019 *J. Power Sources* **438** 226976
[21] Santoro A, D'Antonio P and Caulder S M 1983 *J. Electrochem. Soc.* **130** 1451–9
[22] Moseley P T, Hutchison J L, Wright C J, Bourke M A M, Hill R I and Rainey V S 1983 *J. Electrochem. Soc.* **130** 829–34
[23] Pavlov D 2017 Lead alloys and grids. Grid design principles *Lead-Acid Batteries: Science and Technology* (Elsevier) pp 169–243
[24] Dahodwalla H and Herat S 2000 *J. Clean. Prod.* **8** 133–42
[25] Yang J, Hu C, Wang H, Yang K, Liu J B and Yan H 2017 *Int. J. Energy Res.* **41** 336–52
[26] Seikh A H, Sherif E S M, Mohammed S M A K, Baig M, Alam M A and Alharthi N 2018 *PLoS One* **13** e0195224
[27] Muneret X, Gobe V and Partington K 2007 Corrosion resistance and cycling behaviour of pure lead gravity cast thick plate AGM VRLA reserve power batteries *INTELEC 07–29th Int. Telecommunications Energy Conf.*
[28] Kis Z, Szentmiklósi L, Belgya T, Balaskó M, Horváth L Z and Maróti B 2015 *Phys. Proc.* **69** 40–47
[29] Boovaragavan V, Methakar R N, Ramadesigan V and Subramanian V R 2009 *J. Electrochem. Soc.* **156** A854–62
[30] Pavlov D 2017 Soaking of cured plates before formation *Lead-Acid Batteries: Science and Technology* (Elsevier) pp 425–60
[31] Monahov B and Pavlov D 1994 *J. Electrochem. Soc.* **141** 2316–26
[32] Yolshina L A, Yolshina V A, Yolshin A N and Plaksin S V 2015 *J. Power Sources* **278** 87–97
[33] Meyers J P, Caballes de Guzman R, Swogger S W, McCarrell C, McPherson J, Guan J, Jungman J, Celoria A M, Sugumaran N and Everill P 2020 *J. Energy Storage* **32** 101983
[34] Pavlov D 2017 Curing of battery plates *Lead-Acid Batteries: Science and Technology* (Elsevier) pp 381–421
[35] Davoren B and Ferg E E 2023 *J. Energy Storage* **64** 107165
[36] Mayo M J and Nix W D 1988 *Acta Metall.* **36** 2183–92

[37] Pavlov D, Petkova G, Dimitrov M, Shiomi M and Tsubota M 2000 *J. Power Sources* **87** 39–56

[38] Simon A C 1967 *J. Electrochem. Soc.* **114** 1–8

[39] Gad-Allah A G, El-Rahman H A A, Salih S A and El-Galil M A 1992 *J. Appl. Electrochem.* **22** 571–6

[40] Hollenkamp A F, Constanti K K, Koop M J and Apăteanu L 1992 *J. Power Sources* **48** 195–215

[41] Prengaman R D 1997 *J. Power Sources* **67** 267–78

[42] Ball R J, Kurian R, Evans R and Stevens R 2002 *J. Power Sources* **111** 23–38

[43] Rocca E, Bourguignon G and Steinmetz J 2006 *J. Power Sources* **161** 666–75

[44] Pavlov D 2017 Valve-regulated lead–acid (VRLA) batteries *Lead-Acid Batteries: Science and Technology* (Elsevier) pp 593–620

[45] Mahato B K 1997 *J. Electrochem. Soc.* **126** 365–74

[46] Towarek A, Mistewicz A, Pilecka-Pietrusińska E A, Zdunek J and Mizera J 2022 *J. Archaeol. Sci. Rep.* **45** 103611